

Article

Contribution of Magnetization Mechanisms in MnZn Ferrites with Different Grain Sizes and Sintering Densification

Hai Liu ^{1,2,*}, Jihong Liao ¹, Chonghua Li ³ and Gang Huang ³

¹ Hubei Key Laboratory of Low Dimensional Optoelectronic Materials and Devices, Hubei University of Arts and Science, Xiangyang 441053, China

² School of Materials and Energy, University of Electronic Science and Technology of China, Chengdu 610054, China

³ Hubei Huaci Electronic Technology Co., Ltd., Xiangyang 441053, China

* Correspondence: xiaomingever@gmail.com

Abstract: This study investigates the magnetization mechanisms in MnZn ferrites, which are key materials in high-frequency power electronics, to understand their behavior under various sintering conditions. Employing X-ray diffraction and scanning electron microscopy, we analyzed the microstructure and phase purity of ferrites sintered at different temperatures. Our findings confirm consistent spinel structures and highlight significant grain-growth and densification variabilities. Magnetic properties, particularly the saturation magnetization (M_s) and initial permeability (μ_i), were explored, revealing their direct correlation with the sintering process. The decomposition of magnetic spectra into domain-wall-motion and spin-rotation components offered insights into the dominant magnetization mechanisms, with the domain wall movement becoming increasingly significant at higher sintering temperatures. The samples sintered at 1310 °C showcased superior permeability and the least loss in our investigations. This research underscores the impact of sintering conditions on the magnetic behavior of MnZn ferrites, providing valuable guidelines for optimizing their magnetic performance in advanced electronic applications and contributing to the material science field's understanding of the interplay between sintering, microstructures, and magnetic properties.

Keywords: magnetic material; permeability spectrum; ferrite; power loss



Citation: Liu, H.; Liao, J.; Li, C.;

Huang, G. Contribution of Magnetization Mechanisms in MnZn Ferrites with Different Grain Sizes and Sintering Densification. *Coatings* **2024**, *14*, 302. <https://doi.org/10.3390/coatings14030302>

Academic Editor: Emerson Coy

Received: 17 January 2024

Revised: 27 February 2024

Accepted: 28 February 2024

Published: 29 February 2024



Copyright: © 2024 by the authors. Licensee MDPI, Basel, Switzerland. This article is an open access article distributed under the terms and conditions of the Creative Commons Attribution (CC BY) license (<https://creativecommons.org/licenses/by/4.0/>).

1. Introduction

In the current landscape of power electronics, shaped by the rapid proliferation of 5G technology and the surge in new energy vehicles, there is a profound shift towards high power and a compact design in power-related products [1–4]. This shift prominently features in switch-mode power supplies and communication energy storage systems [5,6]. In coatings, MnZn ferrite is utilized for its electromagnetic shielding properties to absorb and mitigate electromagnetic interferences in electronic device enclosures, for frequency filtering in communication equipment to enhance the signal quality, and for augmenting surface magnetism in applications like magnetic tags or storage media, leveraging its unique magnetic permeability and loss characteristics across various frequencies [7,8]. In this context, reducing magnetic core losses in inductors and transformers has become a paramount concern.

Most power supplies currently operate in the 200 kHz to 3 MHz frequency range, predominantly employing ferrite core materials [9–15]. The inductive reactance, represented as $j\omega L$, implies that as operating frequencies (ω) increase, the required inductance values (L) decrease. This necessitates a balance between achieving higher frequencies and maintaining miniaturization. The key challenge in this scenario is mitigating the escalating magnetic losses at high frequencies [16–20].

There is a pressing need for innovation in magnetic core materials, especially in the 100 kHz to 1 MHz range. A precise analysis of magnetic losses is crucial in developing

MnZn ferrite cores that exhibit lower losses at these frequencies. The trend towards miniaturization in electronic devices also brings to the fore the issue of heat accumulation and temperature rises, making loss reduction at a wide range of temperatures increasingly relevant [21,22]. This study aims to address these challenges, focusing on reducing the magnetic losses in MnZn ferrite cores within the 100 kHz to 1 MHz range, which is pivotal for the next generation of high-frequency power supplies.

M. Marracci et al. conducted a comprehensive study on the temperature-dependent hysteresis losses in minor hysteresis loops, covering a temperature range from $-32\text{ }^{\circ}\text{C}$ to $110\text{ }^{\circ}\text{C}$ [23]. Their research revealed a non-linear trend in these losses, which was attributable to the intricate interplay between exchange energy and magnetic crystalline anisotropy. In a subsequent study, J. Töpfer et al. focused on the influence of various composite additives (CaO, SiO₂, Nb₂O₅, ZrO₂, V₂O₅, and SnO₂) on the core losses of MnZn ferrites [24]. Through a wet chemical synthesis method, they successfully refined the microstructure of MnZn ferrites, achieving a grain size of 4–5 μm , which significantly reduced the core losses to 55 kW/m^3 under conditions of a frequency of 1 MHz, a magnetic field of 25 mT, and a temperature of $80\text{ }^{\circ}\text{C}$.

Ke Sun's research shed light on ion occupancy in Ni-substituted MnZn ferrites, particularly focusing on their Brillouin function temperature characteristics [25]. This study found a distinct preference for Zn²⁺ and Ni²⁺ ions to occupy tetrahedral (A-site) and octahedral (B-site) positions, respectively, with a Mn²⁺ to Fe³⁺ ion ratio of 4:1 in these sites.

Furthermore, K. Praveena's work involved the synthesis of high-frequency (1 MHz) low-loss MnZn ferrites using the combustion method. The findings indicate that increasing the Zn²⁺ content led to a decrease in saturation magnetization and remanence and that optimizing the Zn²⁺ content was key to achieving low losses at 1 MHz. These studies collectively contribute significant insights into the development of MnZn ferrites for high-frequency applications [26].

In summary, among the studies focusing on magnetic properties, composition, additives, sintering processes, and the spectra of complex permeability [27–33], few have delved into the contribution of magnetization mechanisms in MnZn ferrites as a function of grain size and its relationship with the sintering temperature. This research presents an exploration of the magnetization mechanisms in MnZn ferrites at different sintering temperatures, discussing the findings in conjunction with the fitting results of permeability spectrum dispersion. Low-loss MnZn ferrites, applied through tape-casting, co-fired coating, and sol-gel particulate coating, enhance electromagnetic shielding and thin-film inductors in electronics, aiding device miniaturization and performance. Sintered via ceramic oxidation, these ferrites are ideal for magnetron sputtering and pulsed laser deposition, advancing the integration of superior magnetic materials into thin films.

2. Materials and Methods

MnZn ferrites, composed of 55 mol% of Fe₂O₃, 34 mol% of MnO, and 11 mol% of ZnO, were synthesized via the conventional ceramic oxidation method. Initially, the powders were mixed in precise stoichiometric ratios in planetary mills with stainless steel balls for an hour, followed by calcination at $850\text{ }^{\circ}\text{C}$ for two hours in the air. The calcined powders were then doped with 0.02 wt% of Bi₂O₃ and 0.03 wt% of V₂O₅ as a co-solvent to reduce the sintering temperature and were subjected to a second milling for two hours. Post-milling, the powders were dried at $90\text{ }^{\circ}\text{C}$, were granulated with 10 wt% of polyvinyl colloid, and were compressed into toroids ($\Phi 20\text{ mm} \times \Phi 10\text{ mm} \times h 5\text{ mm}$) at a pressure of 20 MPa.

The toroids were sintered at five different temperatures, $1280\text{ }^{\circ}\text{C}$ (labeled $x = 1$), $1290\text{ }^{\circ}\text{C}$ ($x = 2$), $1300\text{ }^{\circ}\text{C}$ ($x = 3$), $1310\text{ }^{\circ}\text{C}$ ($x = 4$), and $1320\text{ }^{\circ}\text{C}$ ($x = 5$), for two hours. Select sintered toroids were processed into spheres with a diameter ranging from 1.2 mm to 1.8 mm to measure their saturation magnetization (M_s).

The crystalline structure of the materials was analyzed using an X-ray diffractometer (XRD-7000, Cu target, 40 kV, 40 mA, K α radiation, Shimadzu Corporation, Kyoto, Japan), and the cross-sectional microstructure was examined using a scanning electron

microscope (SEM, JEOL JSM-6490LV, Akishima, Japan), with the grain size determined by the interception method throughout several photos. The magnetic permeability (μ) and power loss were measured using a B-H analyzer (Iwastu SY-8232, Tokyo, Japan). The measurement of the magnetic permeability spectrum was also conducted using an SY8232, employing a frequency sweep method, under the test conditions of 1 A/m and a frequency of 1 kHz at room temperature. The measurements of saturation magnetization (M_s) and coercive force (H_c) were conducted using a Vibrating Sample Magnetometer (VSM, Lake Shore 8604, Westerville, OH, USA). The Archimedean method was employed for density (d) measurements.

3. Results

Figure 1 displays the XRD patterns of the samples sintered at varying temperatures. These XRD measurements reveal that all samples exhibit a characteristic spinel structure without any impurity phases (JCPDS Card No. 074-2401). The calculated XRD densities (d_{XRD}) for these samples are detailed in Table 1. The theoretical XRD density (d_{XRD}) of MnZn ferrites can be calculated as 5.19 g/cm^3 using the formula $d_{XRD} = 8M/Na^3$, where M represents the molar mass of these MnZn ferrite samples, which is determined from its molecular formula. In the solid-state sintering process, it is anticipated that the reactants will entirely convert into ferrite material. Based on the proportions of the reactants, the final chemical formula of the ferrite is designated as $\text{Mn}_{0.66}\text{Zn}_{0.20}\text{Fe}_{2.14}\text{O}_4$, with a molar mass (M) of 232.8 g/mol. The lattice constant ' a ' was derived from XRD diffraction peaks using the JADE 6.5.26 software and was determined to be 8.4150 Å. ' N ' represents Avogadro's number.

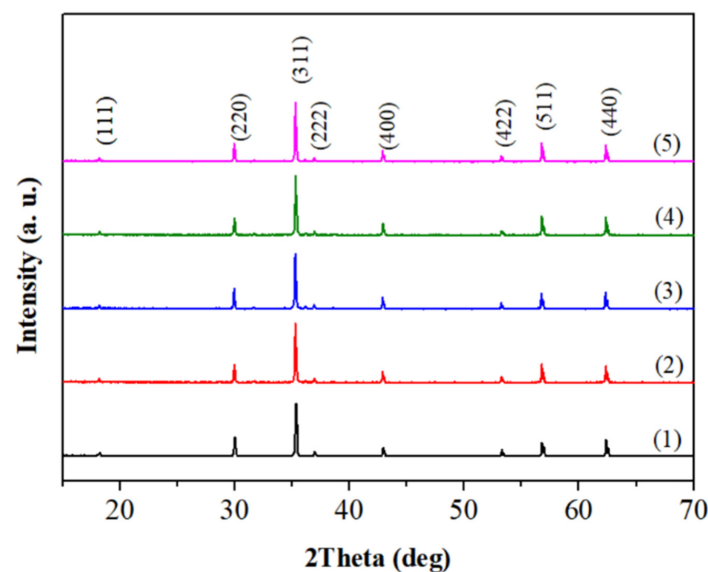


Figure 1. X-ray diffraction results of MnZn ferrite samples.

Table 1. Elemental properties of MnZn ferrites sintered at different temperatures.

Sample No.	D (μm)	μ_i ($f = 1 \text{ kHz}$)	M_s (kA/m^3)	H_c (kA/m)	d (g/cm^3)	P (%)
1	3.7	2794	440	3	5.09	1.9
2	5.5	2796	442	3	5.11	1.5
3	8.9	2961	441	2	5.11	1.5
4	11.5	3097	441	3	5.10	1.7
5	14.1	2996	439	5	5.07	2.3

The sintering density (d) of the MnZn ferrites was measured using the Archimedean method, and porosity (P) was calculated as $P = (d_{XRD} - d)/d_{XRD} \times 100\%$. The sintering

density (d) of MnZn ferrite increases progressively from 1280 °C to 1300 °C, while its XRD density remains constant as an intrinsic property, underscoring the role of solid-state reaction completion in densification. Beyond 1310 °C, a reduction in density and an increase in porosity were observed, peaking at 1300 °C, where the MnZn ferrite attains its maximum densification and optimal microstructure. Figure 2 presents the cross-sectional scanning electron microscopy (SEM) images of the MnZn ferrites. This reduction of porosity (P) is attributed to the concurrent decrease in pore presence at the grain boundaries and the augmentation in grain size.

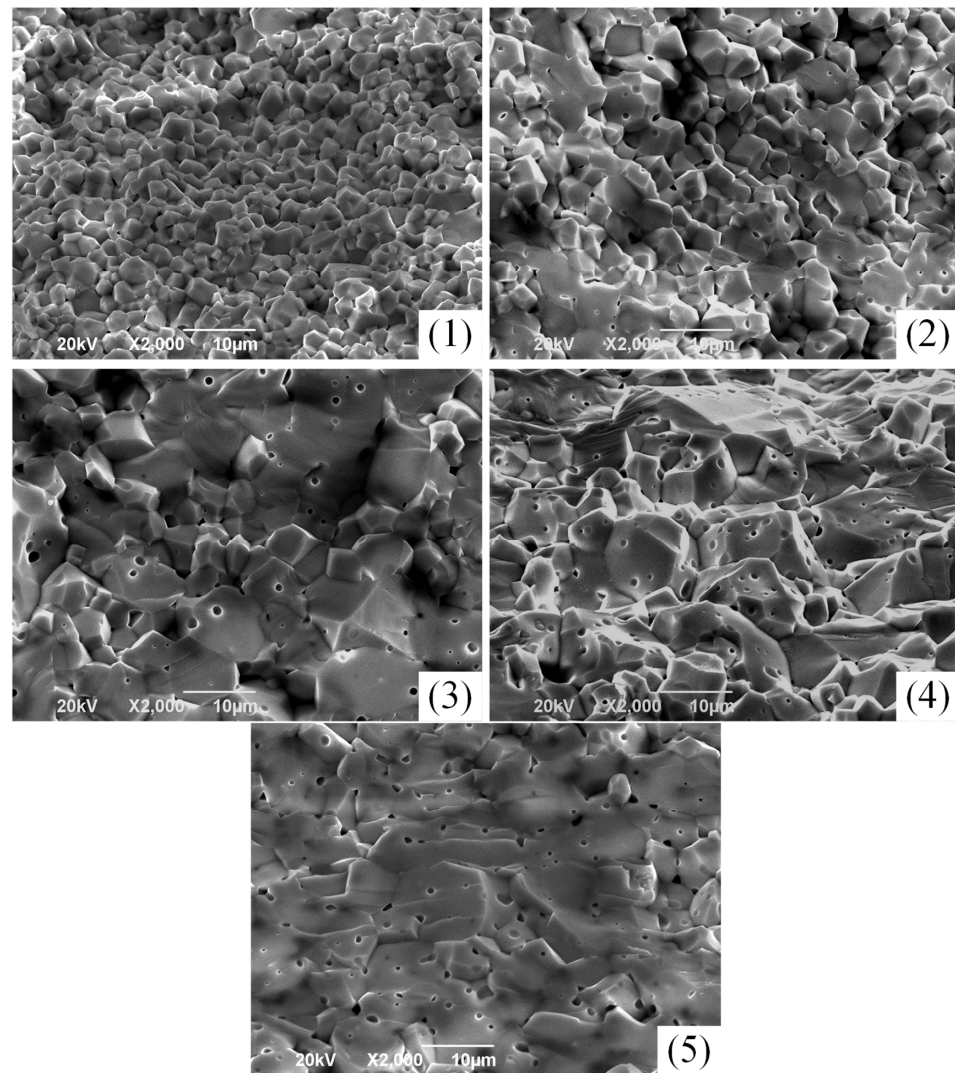


Figure 2. SEM images of MnZn ferrite samples at various sintering temperatures.

With increments in the sintering temperature, a noticeable grain growth is observed in Figure 2. In sample 1, intergranular porosity predominantly resides at the grain boundaries. As the sintering temperature reaches 1290 °C, the microstructure becomes denser, due to the formation of a larger liquid phase within the system. However, abnormal grain growth becomes evident when exceeding 1310 °C. At this temperature, the grains no longer maintain a granular shape but become adhesive, with larger pores appearing within the grains, leading to an increase in porosity (P). The grain size (D) in Table 1 was measured and statistically analyzed using the intercept method under lower-resolution imaging.

Table 1 presents the elemental properties of the MnZn ferrites, detailing the fundamental characteristics of samples 1 through 5. M_s (saturation magnetization) is primarily influenced by densification and intrinsic molecular magnetic moments. Given the con-

stancy of molecular magnetic moments, which is dependent solely on the compositional formula, an increase in densification will enhance the concentration of magnetic moments per unit volume. Consequently, the variation in M_s closely aligns with changes in the sintering density in this study.

The Initial permeability, μ_i , is governed by the equilibrium between the magnetization driving force, which is represented by the saturation magnetization M_s , and the resistance caused by anisotropy and internal stress. The anisotropy is characterized by the anisotropy constant K_1 , while the internal stress is associated with porosity (P).

In Table 1, the magnetic permeability exhibits variations far exceeding those of related physical properties like saturation magnetization and porosity. This discrepancy necessitates an analysis based on the magnetization mechanisms of the material. In magnetic materials, two primary magnetization mechanisms—the domain rotation and the domain wall motion—collectively determine the magnitude of magnetic permeability. This is why permeability is considered a non-intrinsic physical quantity in magnetic materials. When the grain size (D) in a ferromagnetic material exceeds a critical dimension, it transitions from a single-domain to a multi-domain structure, leading to an increase in the number of magnetic domains within each grain.

The average grain size (D) of the samples sintered at different temperatures was determined to be 3.7 μm , 5.5 μm , 8.9 μm , 11.5 μm , and 14.1 μm , respectively. The variation in the number of domain walls, transitioning from single-domain to multi-domain states, significantly impacted the relative contributions of the magnetization mechanisms, leading to anomalous trends in permeability. Magnetic permeability spectrum separation distinguishes between the domain rotation, where individual magnetic moments within a domain reorient towards an external magnetic field, and the domain wall motion, where the boundaries between domains shift to realign the overall magnetization.

To assess and quantitatively describe the influence of the domain wall quantity on permeability in ferrites, a nonlinear least squares method was employed to fit and decompose the magnetic spectra, and the dispersed results are depicted in Figure 3. Considering that the numerical results are already detailed in Table 2, this figure only presents a plot for a single sample (sample 3) as an example.

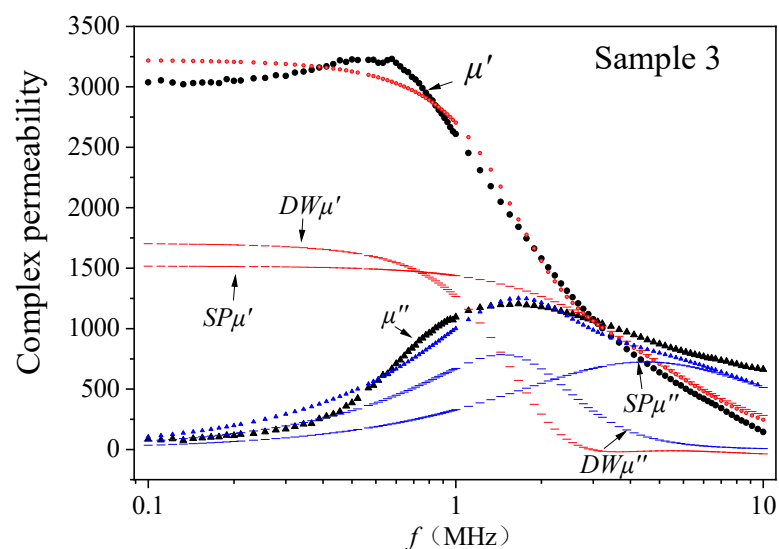


Figure 3. The permeability spectra dispersion of MnZn ferrite for sample 3. The real and imaginary components of the magnetic spectrum are denoted by black spheres and black triangles, respectively. Fitted values for these components, corresponding to two distinct magnetization mechanisms, are depicted by red and blue dashed lines for the real and imaginary parts, respectively. The aggregate values of the magnetic spectrum's real and imaginary parts are illustrated by red spheres and blue triangles, respectively.

Table 2. Permeability spectrum fitting parameters of MnZn ferrites.

No.	χ_{d0}	χ_{s0}	α	$\beta (\times 10^8)$	ω_d ($\times 10^8$ Hz)	ω_s ($\times 10^8$ Hz)	$\omega_{\mu''(\max)}^{DW}$ ($\times 10^7$ Hz)	$\omega_{\mu''(\max)}^{SP}$ ($\times 10^7$ Hz)
1	1536	1454	26.1	0.13	0.13	7.9	2.18	2.72
2	1637	1339	26.4	0.15	0.13	7.6	1.33	2.81
3	1701	1316	24.7	0.15	0.11	6.4	1.22	4.75
4	1742	1289	19.5	0.10	0.08	4.3	2.20	6.47
5	1663	1471	20.6	0.11	0.09	4.8	1.52	5.24

To isolate the contributions of the two magnetization mechanisms, the spectra were separated into domain-wall-motion and domain-rotation components. The complex permeability is expressed by Equation (1), where χ_d and χ_s represent the susceptibilities of domain wall displacement and domain rotation mechanisms, respectively; ω_d and ω_s are their respective cut-off frequencies; χ_{d0} and χ_{s0} are the static susceptibilities of each component; β and α are the damping coefficients; and ω is the actual operating frequency [34–36].

$$\mu = 1 + \chi_d + \chi_s = 1 + \frac{\omega_d^2 \chi_{d0}}{\omega_d^2 - \omega^2 + i\omega\beta} + \frac{(\omega_s + i\omega\alpha)\omega_s \chi_{s0}}{(\omega_s + i\omega\alpha)^2 - \omega^2} \quad (1)$$

To compute the real and imaginary parts of the magnetic spectra, their expressions were derived from Equation (1), as shown in Equations (2) and (3).

$$\mu' = 1 + \frac{\omega_d^2 \chi_{d0} (\omega_d^2 - \omega^2)}{(\omega_d^2 - \omega^2)^2 + \omega^2 \beta^2} + \frac{\chi_{s0} \omega_s^2 [(\omega_s^2 - \omega^2) + \omega^2 \alpha^2]}{[\omega_s^2 - \omega^2(1 + \alpha^2)]^2 + 4\omega^2 \omega_s^2 \alpha^2} \quad (2)$$

$$\mu'' = \frac{\chi_{d0} \beta \omega \omega_d^2}{(\omega_d^2 - \omega^2)^2 + \omega^2 \beta^2} + \frac{\chi_{s0} \omega_s \omega \alpha [\omega_s^2 + \omega^2(1 + \alpha^2)]}{[\omega_s^2 - \omega^2(1 + \alpha^2)]^2 + 4\omega^2 \omega_s^2 \alpha^2} \quad (3)$$

Numerical fitting of the imaginary part of the spectra was conducted, with the fitting parameters used to generate the real part. Good fitting results were achieved under the assumption that each spectrum comprises contributions from both a resonance-type domain wall motion and a relaxation-type domain rotation. The corresponding fitting parameters are listed in Table 2, where $\omega_{\mu''(\max)}^{DW}$ and $\omega_{\mu''(\max)}^{SP}$ correspond to the resonance frequencies of the μ_{DW} - f and μ_{SP} - f spectra, respectively. The resonance frequencies were determined by solving in Equation (1) for these extreme values, as depicted in Equations (4) and (5).

$$\omega_{\mu''(\max)}^{SP} = \omega_s / \sqrt{1 + \alpha^2} \quad (4)$$

$$\omega_{\mu''(\max)}^{DW} = \frac{1}{6} \sqrt{12\omega_d^2 - 6\beta^2 + 6\sqrt{16\omega_d^4 - 4\omega_d^2 \beta^2 + \beta^4}} \quad (5)$$

Besides the good agreement between the computed and experimental curves shown in Figure 3, the accuracy of the fitting parameters was further substantiated by two aspects: (1) the resonance frequency of the domain rotation is significantly higher than that of the domain wall motion, and (2) the fitting results comply with Snoek's Law, as illustrated in Equation (6). This law indicates that the product of initial permeability caused by domain rotation and its resonance frequency, which is determined by the intrinsic properties of the material (γ , gyromagnetic ratio) and M_s , should inversely correlate under minimal variations in a gyromagnetic ratio and M_s . For sample 4, as the magnetic permeability contribution from the domain rotation (χ_{s0}) is the lowest, its corresponding cut-off frequency

$(\omega_{\mu_{(max)}^{SP}})$ will increase accordingly. The fitting results confirm these theoretical expectations for both, affirming the credibility of the fitting methodology and outcomes [37–39].

$$(\mu_i - 1)f_0 = \gamma M_s / 3\pi \quad (6)$$

As the sintering temperature increases, the initial permeability (μ_i) values at 100 kHz are 2794, 2796, 2961, 3097, and 2996, respectively. For a certain magnetization mechanism, permeability is directly proportional to the square of the saturation magnetization (M_s , which is almost invariant in this case) and is inversely proportional to magnetic hindrances, such as internal stress. Notably, the pinning effect of pores within the grains on the domain wall movement is crucial. Therefore, the reduction in permeability in sample 5 can be attributed to an increase in porosity. With rising sintering temperatures, the ratio of χ_{D0} to χ_{S0} evolves as 1.06, 1.22, 1.29, 1.35, and 1.13. As the sintering temperature increases, the contribution ratio of these two components initially rises and then stabilizes, with the domain wall movement emerging as the predominant magnetization mechanism, thereby dominating the changes in permeability. The dominant role of the domain-wall-motion mechanism at various temperatures is also corroborated by the cutoff frequency of the magnetic permeability spectra which is much closer with the domain wall motion part.

Due to the increase in grain size, the domain wall movement becomes a major contributor to dynamic magnetization. In this study, as the sintering temperature rose from 1280 to 1320 °C, the ratio of the contributions from the two magnetization mechanisms, χ_{D0} and χ_{S0} , initially increased but then maintained a decline due to the decline in densification and a pinning effect of the pores. Power loss, which is generally considered an extrinsic property, is known to be influenced by microstructures. However, there has been a long-standing challenge in finding effective methods for its precise quantitative analysis and adjustment. This study's findings provide a deeper understanding of the complex magnetization processes in MnZn ferrites, greatly expanding the current knowledge in this area. Once the magnetization mechanism is clarified, using the well-established relationships between magnetic permeability, microstructure, and power loss, the direct and precise optimization of power loss in MnZn ferrites under various operating conditions by adjusting the microstructure is possible. An accurate measurement of magnetic permeability spectra in soft ferrite thin films has long posed a significant challenge due to large error margins that compromise data analyses of magnetic permeability spectrum separation. Therefore, exploring spectrum separation in sintered bodies, which are the target materials for thin-film fabrication, is crucial for gaining insights into and for quantitatively determining the role of the grain size in the magnetization mechanism.

To further explore the impact of permeability on power loss, the power loss of different samples under various operating temperatures is plotted in Figure 4. This was executed at a frequency of 100 kHz and a magnetic-flux density of 200 mT, which is a typical working condition for high-power applications. At low frequencies, power losses are primarily governed by hysteresis losses, and the hysteresis loss is primarily determined by the magnetic permeability; a higher permeability leads to lower hysteresis losses. For manganese-zinc ferrites, the permeability–temperature (μ - T) relationship initially increases and then decreases (dropping to zero at the Curie temperature). This initial increase results in a unique negative temperature coefficient (NTC) that is characteristic of low-frequency losses in ferrites [40,41]. Conversely, the eddy current and residual losses have positive temperature coefficients, increasing with rising temperatures. The peak of permeability with temperature increases usually occurs between 80–120 °C. As permeability is a non-intrinsic parameter, its curve is not determined by the primary chemical formula of the composition but is greatly influenced by the microstructure of the sintered body. In Figure 4, as the sintering temperature increases, the magnetic permeability initially rises and then declines. Under the NTC effect, in the 80–120 °C range, samples sintered at

1310 °C exhibited the lowest loss. For the samples sintered at 1320 °C, the abundance of intragranular pores pinning the domain walls rendered the domain wall motion irreversible, thereby obscuring the NTC effect.

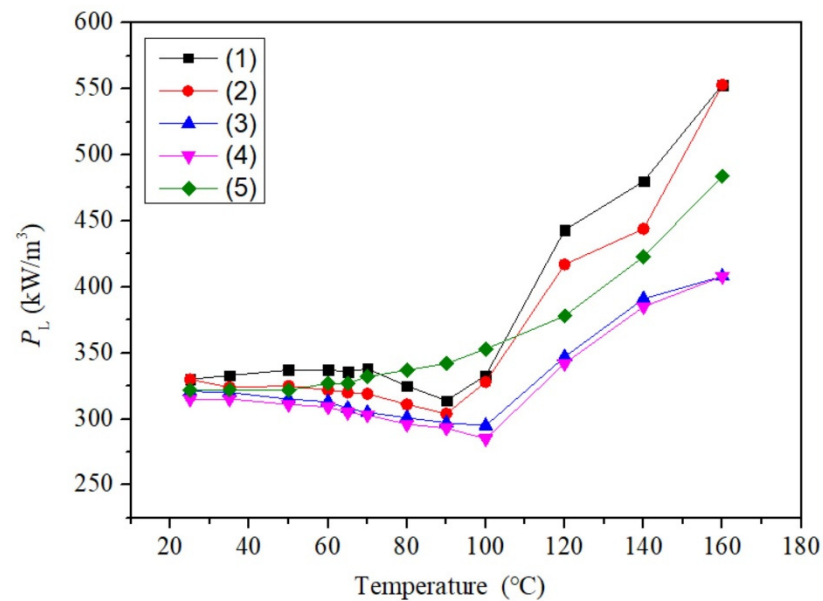


Figure 4. The power loss of different samples under various operating temperatures.

4. Conclusions

This study comprehensively investigates the magnetization mechanisms in MnZn ferrites, emphasizing the effects of the sintering temperature on their microstructural and magnetic properties. XRD analyses confirmed the spinel structure of the samples, while SEM images revealed a significant grain growth and varying degrees of densification. The variation in saturation magnetization (M_s) across most of the samples suggests an interplay between densification and porosity. By dispersing the magnetic spectra into domain-wall-motion and spin-rotation components, this study finds the domain wall movement to be the dominant magnetization mechanism at higher temperatures, as evidenced by the χ_{D0} to χ_{S0} ratio. The samples subjected to sintering at 1310 °C demonstrated optimal permeability and minimal loss. This research provides valuable insights into the magnetic behavior of MnZn ferrites, particularly under varying sintering conditions, contributing to the optimization of their magnetic performance for practical applications.

Author Contributions: Conceptualization, H.L.; data curation, C.L.; methodology, G.H. and J.L.; project administration, J.L.; supervision, G.H.; writing—original draft, H.L.; writing—review and editing, C.L. All authors have read and agreed to the published version of the manuscript.

Funding: We thank the Research and Development Projects in Xiangyang City (project number 2022ABH006835) for funding.

Institutional Review Board Statement: Not applicable.

Informed Consent Statement: Not applicable.

Data Availability Statement: Data are contained within the article.

Conflicts of Interest: Chonghua Li and Gang Huang were employed by the company Hubei Huaci Electronic Technology Co., Ltd. The remaining authors declare that the research was conducted in the absence of any commercial or financial relationships that could be construed as a potential conflict of interest.

References

1. Sai, R.; Shivashankar, S.A.; Yamaguchi, M.; Bhat, N. Magnetic Nanoferrites for RF CMOS: Enabling 5G and Beyond. *Electrochem. Soc. Interface* **2017**, *26*, 71. [CrossRef]
2. Rahman, A.; Yi, N.M.; Ahmed, A.U.; Alam, T.; Singh, M.J.; Islam, M.T. A Compact 5G Antenna Printed on Manganese Zinc Ferrite Substrate Material. *IEICE Electron. Express* **2016**, *13*, 20160377. [CrossRef]
3. Hu, J.; Wen, B.; Burgos, R.; Kang, Y. Design of a Wide-Input-Voltage PCB-Embedded Transformer Based Active-Clamp Flyback Converter Considering Permeability Degradation. *IEEE Trans. Power Electron.* **2021**, *36*, 10355–10365. [CrossRef]
4. Jafari, A.; Samizadeh Nikoo, M.; van Erp, R.; Matioli, E. Optimized Kilowatt-Range Boost Converter Based on Impulse Rectification with 52 kW/l and 98.6% Efficiency. *IEEE Trans. Power Electron.* **2021**, *36*, 7389–7394. [CrossRef]
5. Mathúna, C.O.; Wang, N.; Kulkarni, S.; Roy, S. Review of Integrated Magnetics for Power Supply on Chip (PwrSoC). *IEEE Trans. Power Electron.* **2012**, *27*, 4799–4816. [CrossRef]
6. Di Capua, G.; Femia, N. A Novel Method to Predict the Real Operation of Ferrite Inductors with Moderate Saturation in Switching Power Supply Applications. *IEEE Trans. Power Electron.* **2016**, *31*, 2456–2464. [CrossRef]
7. Wu, S.; Sun, A.; Xu, W.; Zhang, Q.; Zhai, F.; Logan, P.; Volinsky, A.A. Iron-Based Soft Magnetic Composites with Mn–Zn Ferrite Nanoparticles Coating Obtained by Sol–Gel Method. *J. Magn. Magn. Mater.* **2012**, *324*, 3899–3905. [CrossRef]
8. Yavuz, Ö.; Ram, M.K.; Aldissi, M.; Poddar, P.; Hariharan, S. Synthesis and the Physical Properties of MnZn Ferrite and NiMnZn Ferrite–Polyaniline Nanocomposite Particles. *J. Mater. Chem.* **2005**, *15*, 810–817. [CrossRef]
9. Yi, S.; Bai, G.; Wang, X.; Zhang, X.; Hussain, A.; Jin, J.; Yan, M. Development of High-Temperature High-Permeability MnZn Power Ferrites for MHz Application by Nb₂O₅ and TiO₂ Co-Doping. *Ceram. Int.* **2020**, *46*, 8935–8941. [CrossRef]
10. Kalarus, J.; Kogias, G.; Holz, D.; Zaspalis, V.T. High Permeability–High Frequency Stable MnZn Ferrites. *J. Magn. Magn. Mater.* **2012**, *324*, 2788–2794. [CrossRef]
11. Keluskar, S.H.; Tangsali, R.B.; Naik, G.K.; Budkuley, J.S. High Permeability of Low Loss Mn–Zn Ferrite Obtained by Sintering Nanoparticle Mn–Zn Ferrite. *J. Magn. Magn. Mater.* **2006**, *305*, 296–303. [CrossRef]
12. Janghorban, K.; Shokrollahi, H. Influence of V₂O₅ Addition on the Grain Growth and Magnetic Properties of Mn–Zn High Permeability Ferrites. *J. Magn. Magn. Mater.* **2007**, *308*, 238–242. [CrossRef]
13. Su, H.; Zhang, H.; Tang, X.; Wei, X. Effects of Calcining and Sintering Parameters on the Magnetic Properties of High-Permeability MnZn Ferrites. *IEEE Trans. Magn.* **2005**, *41*, 4225–4228. [CrossRef]
14. Zulauf, G.; Tong, Z.; Plummer, J.D.; Rivas-Davila, J.M. Active Power Device Selection in High- and Very-High-Frequency Power Converters. *IEEE Trans. Power Electron.* **2019**, *34*, 6818–6833. [CrossRef]
15. Kollár, P.; Oleksáková, D.; Vojtek, V.; Fúzer, J.; Fáberová, M.; Bureš, R. Steinmetz Law for Ac Magnetized Iron-Phenolformaldehyde Resin Soft Magnetic Composites. *J. Magn. Magn. Mater.* **2017**, *424*, 245–250. [CrossRef]
16. Ying, Y.; Hu, L.; Li, Z.; Zheng, J.; Yu, J.; Li, W.; Qiao, L.; Cai, W.; Li, J.; Bao, D.; et al. Preparation of Densified Fine-Grain High-Frequency MnZn Ferrite Using the Cold Sintering Process. *Materials* **2023**, *16*, 3454. [CrossRef]
17. Wu, T.; Wang, C.; Li, Z.; Lan, Z.; Yu, Z.; Du, Y.; Wu, C.; Jiang, X.; Li, Q.; Wang, C.; et al. A Comprehensive Study on MnZn Ferrite Materials with High Saturation Magnetic Induction Intensity and High Permeability for Magnetic Field Energy Harvesting. *J. Magn. Magn. Mater.* **2024**, *590*, 171635. [CrossRef]
18. Li, Z.; Ying, Y.; Wang, N.; Zheng, J.; Yu, J.; Li, W.; Qiao, L.; Cai, W.; Li, J.; Huang, H.; et al. Effect of Compressive Stress on Power Loss of Mn–Zn Ferrite for High-Frequency Applications. *Ceram. Int.* **2022**, *48*, 17723–17728. [CrossRef]
19. Xu, Z.; Fan, J.; Liu, T.; Han, Y.; Zhang, H. Calcination Induced Phase Transformation in MnZn Ferrite Powders. *J. Alloys Compd.* **2020**, *814*, 152307. [CrossRef]
20. Bhandare, S.V.; Kumar, R.; Anupama, A.V.; Choudhary, H.K.; Jali, V.M.; Sahoo, B. Mechanistic Insights into the Sol-Gel Synthesis of Complex (Quaternary) Co–Mn–Zn-Spinel Ferrites: An Annealing Dependent Study. *Ceram. Int.* **2020**, *46*, 17400–17415. [CrossRef]
21. Xu, Z.; Yu, Z.; Sun, K.; Li, L.; Ji, H.; Lan, Z. Microstructure and Magnetic Properties of Sn-Substituted MnZn Ferrites. *J. Magn. Magn. Mater.* **2009**, *321*, 2883–2889. [CrossRef]
22. Zhou, X.; Wang, J.; Zhou, L.; Yao, D. The Improved Saturation Magnetization and Initial Permeability in Mn–NiZn Ferrites after Cooling in Vacuum. *Appl. Phys. A* **2022**, *128*, 306. [CrossRef]
23. Marracci, M.; Tellini, B. Hysteresis Losses of Minor Loops versus Temperature in MnZn Ferrite. *IEEE Trans. Magn.* **2013**, *49*, 2865–2869. [CrossRef]
24. Töpfer, J.; Angermann, A. Complex Additive Systems for Mn-Zn Ferrites with Low Power Loss. *J. Appl. Phys.* **2015**, *117*, 17A504. [CrossRef]
25. Sun, K.; Wu, C.; Yang, Y.; Yu, Z.; Guo, R.; Wei, P.; Jiang, X.; Lan, Z. Cation Distribution and Temperature Dependence of Brillouin Function for Nickel-Substituted Manganese–Zinc Ferrites. *IEEE Trans. Magn.* **2015**, *51*, 6301304. [CrossRef]
26. Praveena, K.; Chen, H.-W.; Liu, H.-L.; Sadhana, K.; Murthy, S.R. Enhanced Magnetic Domain Relaxation Frequency and Low Power Losses in Zn²⁺ Substituted Manganese Ferrites Potential for High Frequency Applications. *J. Magn. Magn. Mater.* **2016**, *420*, 129–142. [CrossRef]
27. Yang, Y.; Yu, Z.; Guo, Q.; Sun, K.; Guo, R.; Jiang, X.; Liu, Y.; Liu, H.; Wu, G.; Lan, Z. Thermomagnetization Characteristics and Ferromagnetic Resonance Linewidth Broadening Mechanism for Ca-Sn Co-Substituted YIG Ferrites. *Ceram. Int.* **2018**, *44*, 11718–11723. [CrossRef]

28. Wu, C.; Wang, W.; Li, Q.; Wei, M.; Luo, Q.; Fan, Y.; Jiang, X.; Lan, Z.; Jiao, Z.; Tian, Y.; et al. Barium Hexaferrites with Narrow Ferrimagnetic Resonance Linewidth Tailored by Site-Controlled Cu Doping. *J. Am. Ceram. Soc.* **2022**, *105*, 7492–7501. [[CrossRef](#)]
29. Dhiman, R.L.; Taneja, S.P.; Reddy, V.R. Structural and Mössbauer Spectral Studies of Nanosized Aluminum Doped Manganese Zinc Ferrites. *Adv. Condens. Matter Phys.* **2009**, *2008*, e839536. [[CrossRef](#)]
30. Siddique, M.; Butt, N.M.; Shafi, M.; Abbas, T.; Misbah, U.-I. Cation Distribution in Ni-Substituted Mn-Ferrites by Mössbauer Technique. *J. Radioanal. Nucl. Chem.* **2003**, *258*, 525–529. [[CrossRef](#)]
31. Wu, G.; Yu, Z.; Guo, R.; Wang, Z.; Wang, H.; Hu, Z.; Liu, M. Effects of Magnetic Domain Morphology on the Magnetic Spectrum and High-Frequency Core Losses of MnZn Ferrites. *J. Am. Ceram. Soc.* **2024**, *107*, 1117–1126. [[CrossRef](#)]
32. Wu, G.; Yu, Z.; Sun, K.; Guo, R.; Wang, B.; Jiang, X.; Li, L.; Lan, Z. Excellent Tunable DC Bias Superposition Characteristics for Manganese–Zinc Ferrites. *IEEE Trans. Power Electron.* **2020**, *35*, 1845–1854. [[CrossRef](#)]
33. Baguley, C.A.; Madawala, U.K.; Carsten, B. The Influence of Remanence on Magnetostrictive Vibration and Hysteresis in Mn-Zn Ferrite Cores. *IEEE Trans. Magn.* **2012**, *48*, 1844–1850. [[CrossRef](#)]
34. Li, Q.; Chen, Y.; Yu, C.; Young, L.; Spector, J.; Harris, V.G. Emerging Magnetodielectric Materials for 5G Communications: 18H Hexaferrites. *Acta Mater.* **2022**, *231*, 117854. [[CrossRef](#)]
35. Li, Q.; Chen, Y.; Li, Q.; Li, L.; Qian, K.; Harris, V.G. Suppressed Domain Wall Damping in Planar BaM Hexaferrites for Miniaturization of Microwave Devices. *J. Magn. Magn. Mater.* **2020**, *514*, 167172. [[CrossRef](#)]
36. Ahns, S.J.; Yoon, C.S.; Yoon, S.G.; Kim, C.K.; Byun, T.Y.; Hong, K.S. Domain Structure of Polycrystalline MnZn Ferrites. *Mater. Sci. Eng. B* **2001**, *84*, 146–154. [[CrossRef](#)]
37. Acher, O.; Adenot, A.L. Bounds on the Dynamic Properties of Magnetic Materials. *Phys. Rev. B* **2000**, *62*, 11324–11327. [[CrossRef](#)]
38. Race, C.P.; Hadian, R.; von Pezold, J.; Grabowski, B.; Neugebauer, J. Mechanisms and Kinetics of the Migration of Grain Boundaries Containing Extended Defects. *Phys. Rev. B* **2015**, *92*, 174115. [[CrossRef](#)]
39. Xing, Y.; Myers, J.; Obi, O.; Sun, N.X.; Zhuang, Y. Excessive Grain Boundary Conductivity of Spin-Spray Deposited Ferrite/Non-Magnetic Multilayer. *J. Appl. Phys.* **2012**, *111*, 07A512. [[CrossRef](#)]
40. Fujita, A.; Gotoh, S. Temperature Dependence of Core Loss in Co-Substituted MnZn Ferrites. *J. Appl. Phys.* **2003**, *93*, 7477–7479. [[CrossRef](#)]
41. Tsutaoka, T. Frequency Dispersion of Complex Permeability in Mn–Zn and Ni–Zn Spinel Ferrites and Their Composite Materials. *J. Appl. Phys.* **2003**, *93*, 2789–2796. [[CrossRef](#)]

Disclaimer/Publisher’s Note: The statements, opinions and data contained in all publications are solely those of the individual author(s) and contributor(s) and not of MDPI and/or the editor(s). MDPI and/or the editor(s) disclaim responsibility for any injury to people or property resulting from any ideas, methods, instructions or products referred to in the content.